

## Supporting Information

### **Metal Coordination Sphere Deformation Induced Highly Stokes-Shifted, Ultra Broadband Emission in 2D Hybrid Lead-Bromide Perovskites and Investigation of Its Origin**

*Benny Febriansyah<sup>+</sup>, Tetiana Borzda<sup>+</sup>, Daniele Cortecchia, Stefanie Neutzner, Giulia Folpini, Teck Ming Koh, Yongxin Li, Nripan Mathews, Annamaria Petrozza,\* and Jason England\**

anie\_201915708\_sm\_miscellaneous\_information.pdf

## Materials synthesis

**Chemicals.** Lead(II) bromide, hydrobromic acid, pyridine, 1-(2-aminoethyl)piperidine, and 2-bromoethan-1-ammonium bromide were purchased from commercial vendors. Acetonitrile was dried with CaH<sub>2</sub> prior to distillation.

**1-(2-Ammonioethyl)pyridin-1-ium dibromide, 1(Br)<sub>2</sub>.** A flamed-dried, two-necked round bottom flask was charged with pyridine (1.05 equivalent), 2-bromoethylammonium bromide (1.00 equivalent), a magnetic stirring bar, and anhydrous acetonitrile. The resulting mixture was heated, with stirring, at reflux until completion of reaction, which took 3 – 4 days. Progress of the reaction was monitored by <sup>1</sup>H NMR spectroscopy. Subsequent to cooling to room temperature, the precipitate formed during reaction was isolated by filtration, thoroughly washed with diethyl ether, and dried under vacuum to give the product as a beige solid (1.52 g, 85% yield). <sup>1</sup>H NMR (400 MHz, DMSO-d<sub>6</sub>): δ 9.14 (d, 2 H, ArH), 8.67 (t, 1 H, ArH), 8.23 (t, 2 H, ArH), 8.18 (bs, 3 H, NH<sub>3</sub><sup>+</sup>), 4.95 (t, 2 H, CH<sub>2</sub>), 3.53 (t, 2 H, CH<sub>2</sub>). <sup>13</sup>C{<sup>1</sup>H} NMR (100 MHz, DMSO-d<sub>6</sub>): δ 146.2, 145.4, 128.3, 57.7, 39.1.

**1-(2-Ammonioethyl)piperidin-1-ium (2) dibromide.** To an ice-cooled round bottom flask containing ethanol and the requisite amine, a stoichiometric amount of concentrated hydrobromic acid was added. After stirring the solution for 1 hour, all volatiles were removed using a rotary evaporator. The solids thereby obtained were washed with copious amounts of diethyl ether and dried under vacuum, at 50°C, overnight. Isolated as a white solid (1.28 g; 88% yield). <sup>1</sup>H NMR (400 MHz, DMSO-d<sub>6</sub>): δ 9.51 (bs, H, NH<sup>+</sup>), 8.08 (bs, 3 H, NH<sub>3</sub><sup>+</sup>), 3.49 (m, 2 H, CH<sub>2</sub>), 3.30 (m, 4 H, CH<sub>2</sub>), 3.02 (m, 2 H, CH<sub>2</sub>), 1.80-1.67 (m, 5 H, CH<sub>2</sub>), 1.42-1.39 (m, H, CH<sub>2</sub>). <sup>13</sup>C{<sup>1</sup>H} NMR (100 MHz, DMSO-d<sub>6</sub>): δ 52.8, 52.7, 33.4, 22.5, 20.9.

**Growth of single crystals of hybrid lead-bromide perovskites.** In general, mixtures of stoichiometric amounts of PbBr<sub>2</sub> and organic bromide salt were added to sufficient volumes of concentrated aqueous HBr to afford Pb<sup>2+</sup> concentrations of 0.25 – 0.33 M. Upon stirring at ~120°C, for approximately 30 mins, clear solutions were obtained. Subsequent *slow* cooling to room temperature afforded crystals suitable for X-ray crystallography. The typical crystallization yield of **1**[PbBr<sub>4</sub>] and **2**[PbBr<sub>4</sub>] are 63% (0.72 g) and 49% (0.55 g), respectively, based on Pb content.

**Thin film fabrication.** Thin films used for UV-vis absorbance and photoluminescence spectroscopic measurements were prepared by the following procedure. 0.50 M solutions of stoichiometric amounts of organic and lead bromide salts, dissolved in DMSO, were spin coated onto pre-cleaned glass substrates at 3000 rpm for 30 s. (The glass substrates were cleaned by sequential 15 minutes sonication in soap solution (Decon), deionized water, ethanol, and acetone, followed by ozone plasma treatment for 15 mins.) The resulting films were, subsequently, heated at 130°C for 10 mins. FE-SEM images (Figure S11) confirm that the films exhibit complete coverage and a pinhole-free morphology.

## Instrumentation and methods

**Nuclear Magnetic Resonance (NMR) spectroscopy.**  $^1\text{H}$  and  $^{13}\text{C}\{^1\text{H}\}$  NMR spectra of organic compounds were recorded in DMSO- $d_6$  solution, using a Bruker Avance 400 spectrometer. Chemical shift values (ppm) are referenced against residual protic solvent peaks.

**X-ray single crystallography.** Crystals were mounted on a Bruker X8 Quest CPAD area detector diffractometer and data was collected using I $\mu$ S 3.0 Microfocus Mo-K $\alpha$  radiation ( $\lambda = 0.71073 \text{ \AA}$ ), at both cryogenic and ambient temperatures (100 and 296 K, respectively). Data reduction and absorption corrections were performed using the SAINT and SADABS software packages, respectively.<sup>1</sup> All structures were solved by direct methods and refined by full-matrix least squares procedures on  $F^2$ , using the Bruker SHELXTL-2014 software package.<sup>2,3</sup> Non-hydrogen atoms were anisotropically refined, after which hydrogen atoms were introduced at calculated positions and the data was further refined. Graphical representations of the crystal structures used throughout the main paper and supporting information were created using the programs Mercury and VESTA.<sup>4</sup>

**Analysis of structural distortions in 2D perovskites.** Distortion of the octahedral  $[\text{PbBr}_6]^{4-}$  building blocks that comprise the inorganic lattice were evaluated using the following parameters:

$$\text{Bond length distortion}^5: \Delta_{oct} = \frac{1}{6} \sum_{i=1}^6 \left[ \frac{d_i - d_m}{d_m} \right]^2 \quad (1)$$

$$\text{Octahedral elongation}^{6,7}: \lambda_{oct} = \frac{1}{6} \sum_{i=1}^6 \left[ \frac{d_i}{d_0} \right]^2 \quad (2)$$

$$\text{Octahedral angle variance}^{5-8}: \sigma_{oct}^2 = \frac{1}{11} \sum_{i=1}^{12} (\alpha_i - 90)^2 \quad (3)$$

where  $d_i$  = Pb–Br bond length,  $d_m$  = average Pb–Br bond length,  $d_0$  = center-to-vertex distance of a regular polyhedron of the same volume, and  $\alpha_i$  = individual Br–Pb–Br angles.

The parameters  $\Delta_{oct}$ ,  $\lambda_{oct}$  and  $\sigma_{oct}^2$  provide a quantitative measure of polyhedral distortion, independent of the effective size of the polyhedron. Whereas the crystallographic software package VESTA was used to calculate the structural distortion parameters  $\lambda_{oct}$  and  $\sigma_{oct}^2$ , the Pb-( $\mu$ -Br)-Pb bond angles between conjoined  $[\text{PbBr}_6]^{4-}$  octahedra were obtained from Mercury.

**Analysis of penetration of the organic cations into the cuboctahedral cavities of the inorganic lattices.** All analysis was performed using the software package Mercury. The boundary of the perovskite cuboctahedral cavities or ‘bay region’ was defined as being the mean plane comprised of the terminal bromide ions, on the same side of the 2D planes, of four nearest neighbour  $[\text{PbBr}_6]^{4-}$  octahedra. The degree of penetration of the aromatic ring moieties (pyridinium and piperidinium) were quantified by measuring the distance between the “para”-carbon atom in the ring and the aforementioned mean planes (see Figures 2c and 2d in the main article). Meanwhile, penetration of the exocyclic primary ammonium is obtained by measuring the distances between the N atoms of the primary ammonium heads and the mean planes.

**UV-vis spectroscopy.** UV-vis absorption spectra were recorded using a SHIMADZU UV-3600 spectrophotometer, with an integrating sphere (ISR-3100), in the wavelength range 200 – 800 nm, a step size of 0.5 nm, and a slow scan speed.

**Raman spectroscopy.** The measurements were performed upon single crystals of perovskite, using a inVia Raman Microscope Renishaw micro-Raman confocal microscope (with a 10 x objective and a 785 nm excitation wavelength). All measurements were performed in air.

**Steady-state temperature- and power-dependent photoluminescence (PL) spectroscopies.** PL was excited at different fluences with a 405 nm Oxxius laser and collected with a Maya 2000 Spectrometer. All measurements were conducted under vacuum, at 77K. All temperature-dependent measurements were performed using an Oxford Instruments cold finger cryostat.

**Field-emission scanning electron microscopy (FE-SEM).** Surface morphology and cross-section images of the 2D perovskite thin films were recorded using a JEOL JSM-7600F FE-SEM, with an accelerating voltage of 5kV.

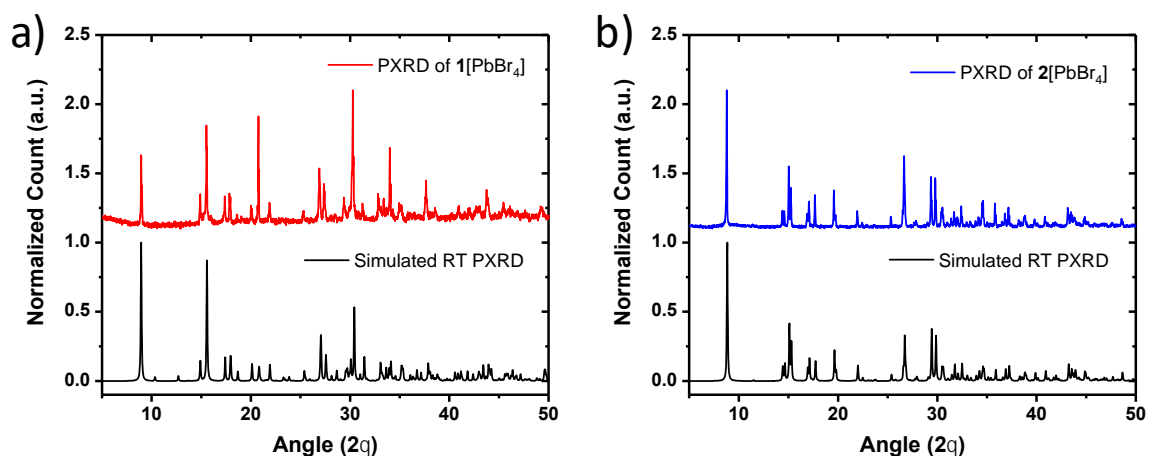
**Time-resolved photoluminescence (TRPL) spectroscopy.** TRPL measurements were performed at 293 and 77K, using a Hamamatsu streak camera and Chameleon laser from Coherent. Excitation at 368 nm, with a fluence  $2.5 \text{ nJ/cm}^2$ , and different repetition rates of 80 and 2 MHz were used. Lifetimes of individual decay components and their contributions to

the overall decay are listed in Table S4. The following equation was used to analyze the temporal PL profile:

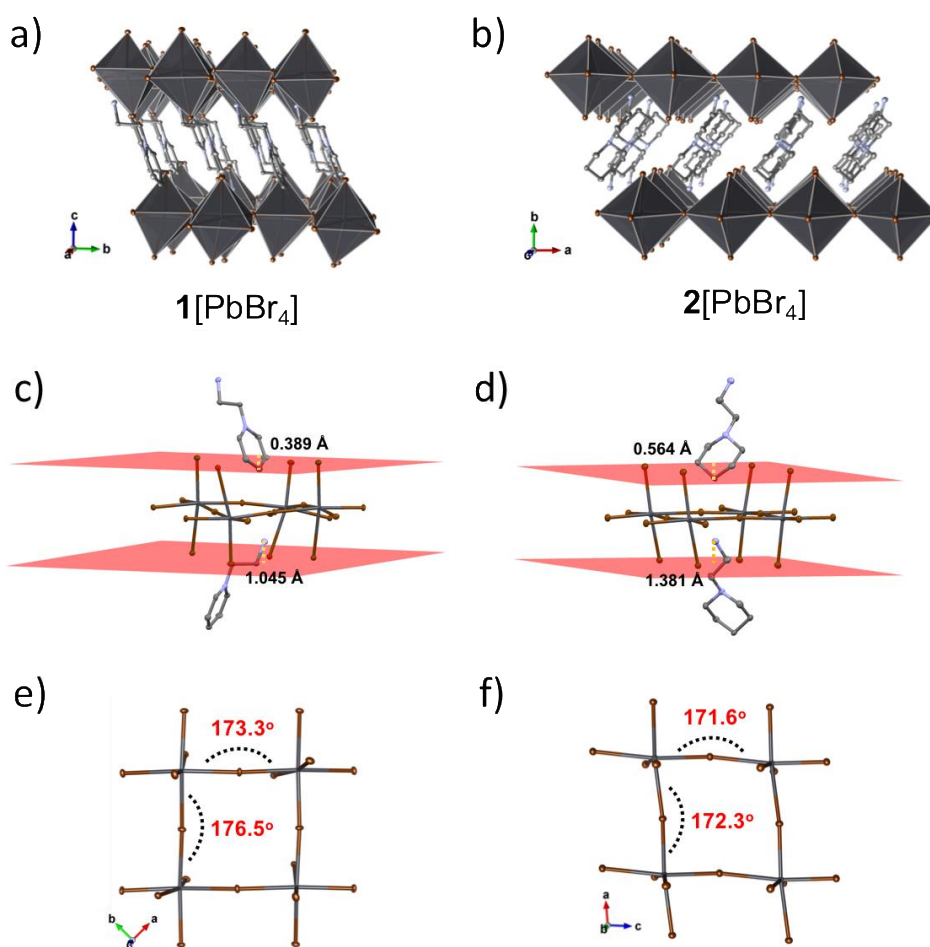
$$I = I_0 * \exp(-t/\tau)^\beta$$

Where  $\tau$  and  $\beta$  are the decay constant and lifetime distribution parameter, respectively.

**Powder X-ray diffraction.** Powder X-ray diffraction measurements were conducted using a Bruker AXS D8 ADVANCE system containing a Cu K $\alpha$  radiation source ( $\lambda = 1.5418 \text{ \AA}$ ). The XRD spectra were recorded with an incident angle of  $5^\circ$ , a step size of  $0.05^\circ$ , and a delay time of 1s for each step.



**Figure S1.** Room temperature powder X-ray diffraction (PXRD) patterns of 2D bromoplumbates (a)  $1[\text{PbBr}_4]$  and (b)  $2[\text{PbBr}_4]$ . For comparison, the simulated room temperature (RT) PXRD patterns are included.

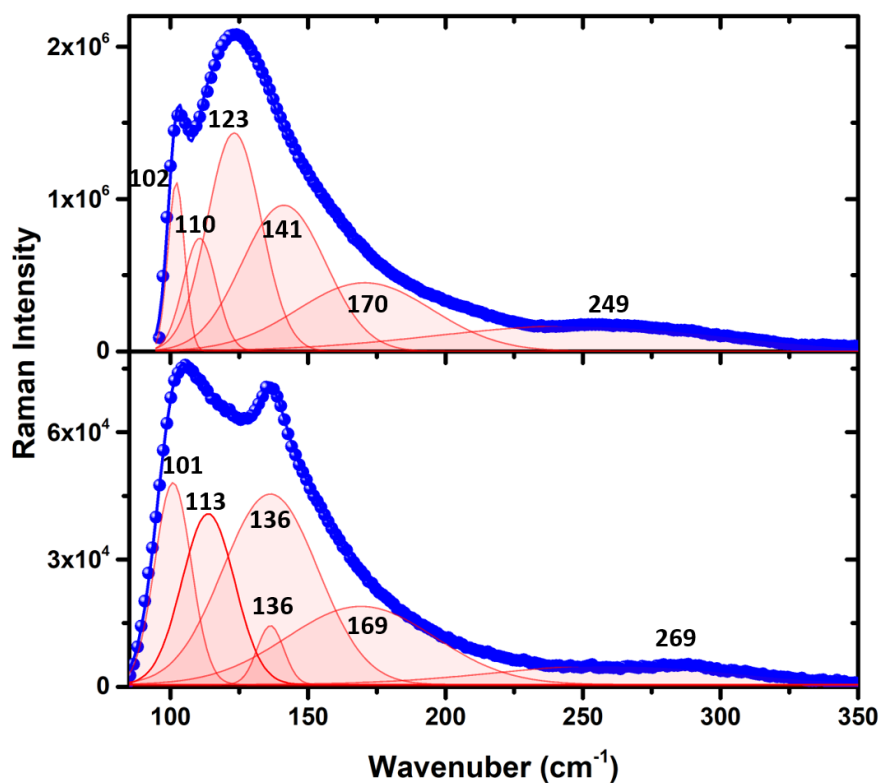


**Figure S2.** X-ray crystal structures of (a)  $1[\text{PbBr}_4]$  and (b)  $2[\text{PbBr}_4]$ , recorded at 100 K. The degree of penetration of the organic dications into the ‘bay regions’ of the 2D perovskites, built from four nearest neighbour  $[\text{PbBr}_6]^{4-}$  octahedra, in (c)  $1[\text{PbBr}_4]$  and (d)  $2[\text{PbBr}_4]$  are delineated using orange dashed lines. Additionally, penetration distances are provided. ‘Top views’ of (e)  $1[\text{PbBr}_4]$  and (f)  $2[\text{PbBr}_4]$ , presented with their respective crystallographic axes, are included to highlight Pb-( $\mu$ -Br)-Pb bond angles (values provided). Black, brown, grey, and blue spheroids represent Pb, Br, C, and N atoms, respectively. H atoms are omitted for clarity. Ellipsoids are shown at 50% probability.

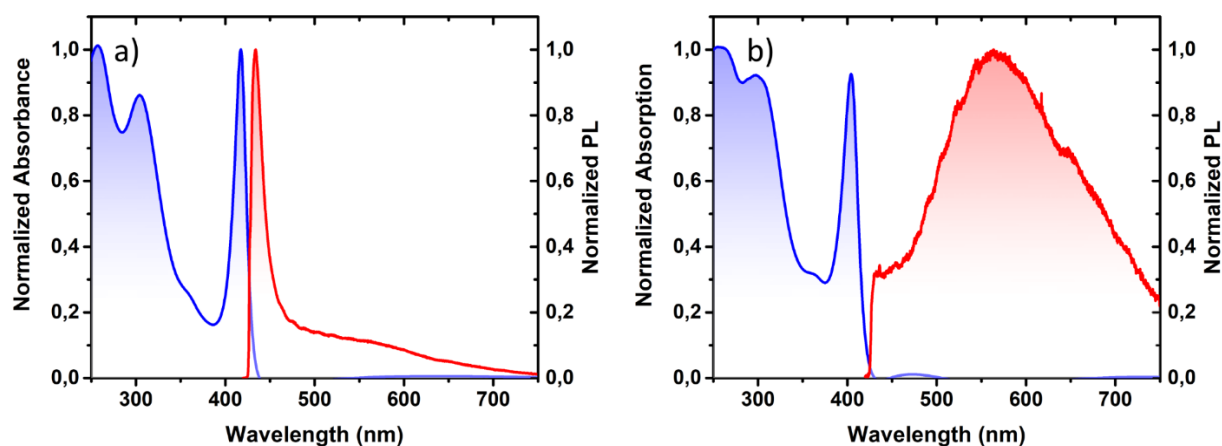
Whereas the bulky ring moieties in  $1[\text{PbBr}_4]$  and  $2[\text{PbBr}_4]$  display minimal penetration into the bay regions of ca. 0.319 and 0.374 Å, respectively, at room temperature (Figure 2c and d), the appended ethylammonium chains are found to insert quite deeply, by ca. 1.095 Å and 1.346 Å, respectively. (As can be seen in Figure S2, the values are marginally different in X-ray structure recorded at 100 K, but the general trends hold true.) The greater penetration of the piperidinium ring of **2**, compared with the pyridinium ring of **1**, is likely a consequence

of its lesser ability to delocalize positive charge and this, combined with its bulkier nature, leads to greater distortion in  $2[\text{PbBr}_4]$  relative to  $1[\text{PbBr}_4]$ . In contrast, in the vast majority of Pb-halide perovskites, all 'bay regions' are occupied by primary ammonium functionality, so the environments of their Pb-Br octahedra are inherently more symmetrical.<sup>9-11</sup> Furthermore, the penetrations of their primary ammonium moieties into the perovskite 'bay regions' are also significantly smaller, with distances of ca. 0.7 Å and below being the norm.<sup>12</sup> This results in small intra-octahedral distortions.

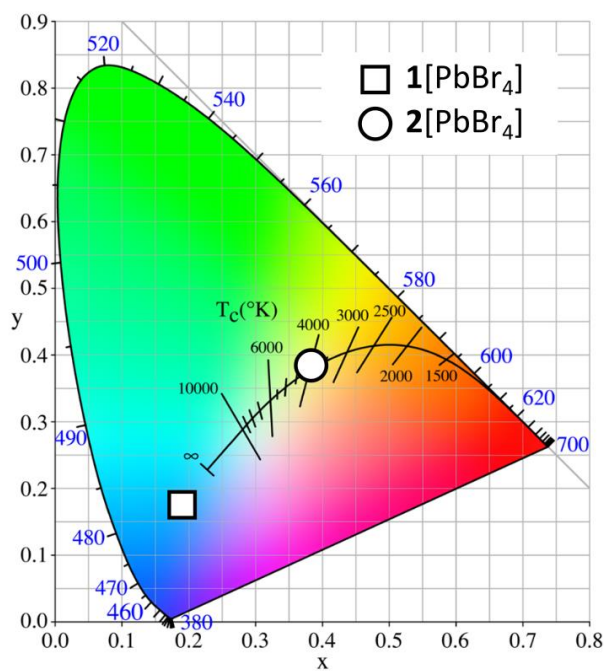




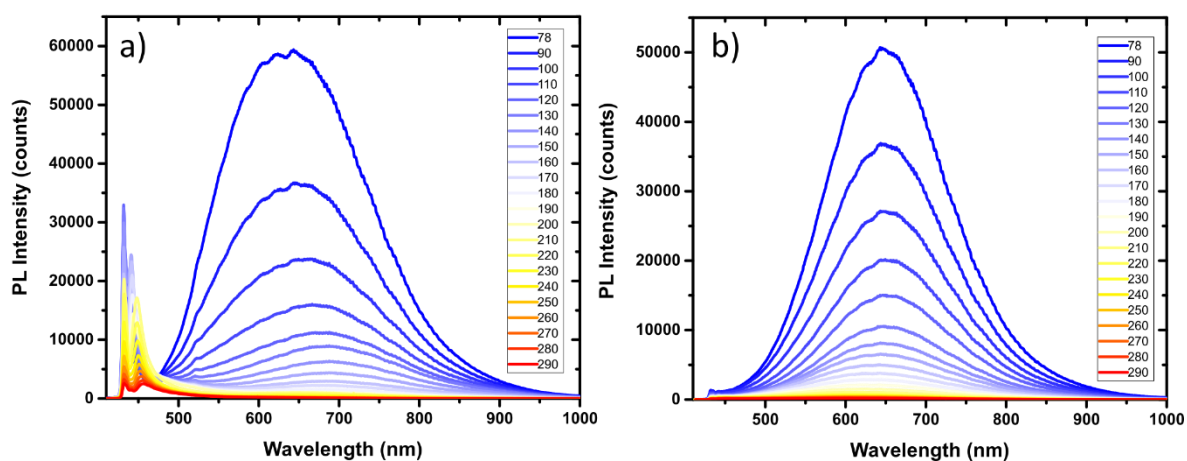
**Figure S3.** Raman spectra of (top)  $2[\text{PbBr}_4]$  and (bottom)  $1[\text{PbBr}_4]$ . The vibrational mode at  $123 \text{ cm}^{-1}$  in  $2[\text{PbBr}_4]$ , which can be attributed to the lurching of the ammonium moieties,<sup>13</sup> shifts to significantly higher wavenumbers ( $\sim 136 \text{ cm}^{-1}$ ) in  $1[\text{PbBr}_4]$ . We correlate such shift to the increased in-plane Pb-Br stretching in  $1[\text{PbBr}_4]$  in comparison to that of  $2[\text{PbBr}_4]$ , which is likely to be caused by shorter average Pb-Br<sub>eq</sub> bond lengths in the latter (Table S5).



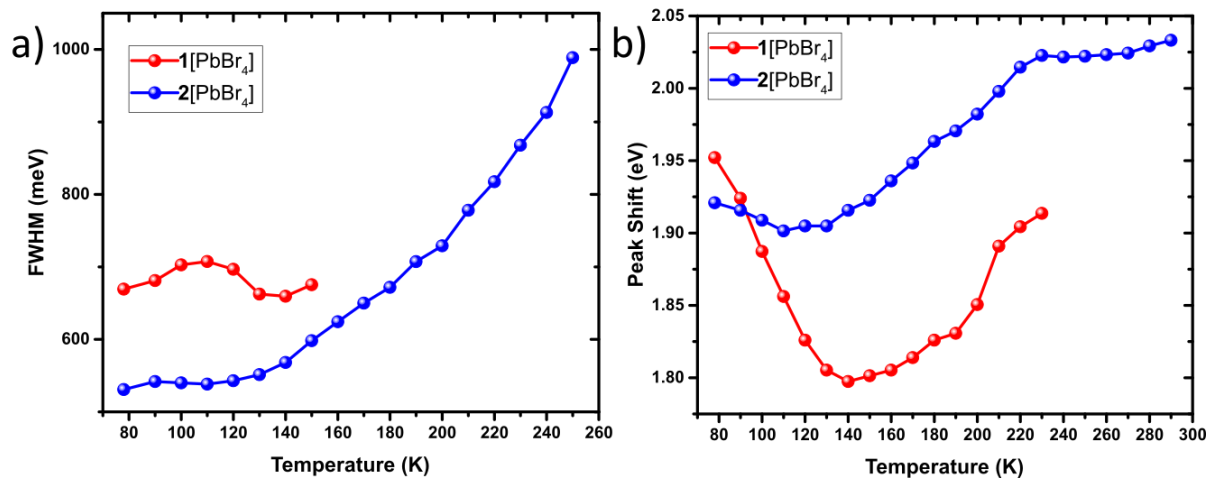
**Figure S4.** Absorption (blue line) and photoluminescence (red line) spectra of thin films of a)  $1[\text{PbBr}_4]$  and b)  $2[\text{PbBr}_4]$ .



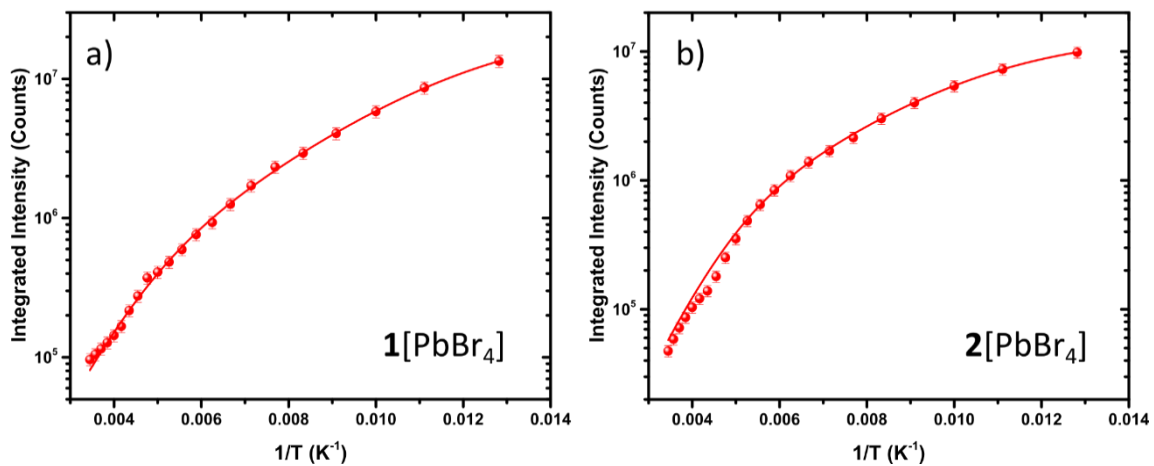
**Figure S5.** CIE chromaticity diagram and coordinates for the room temperature emission of **1**[PbBr<sub>4</sub>] (0.19; 0.17) and **2**[PbBr<sub>4</sub>] (0.38; 0.38), upon excitation at  $\lambda_{\text{exc}} = 405$  nm.



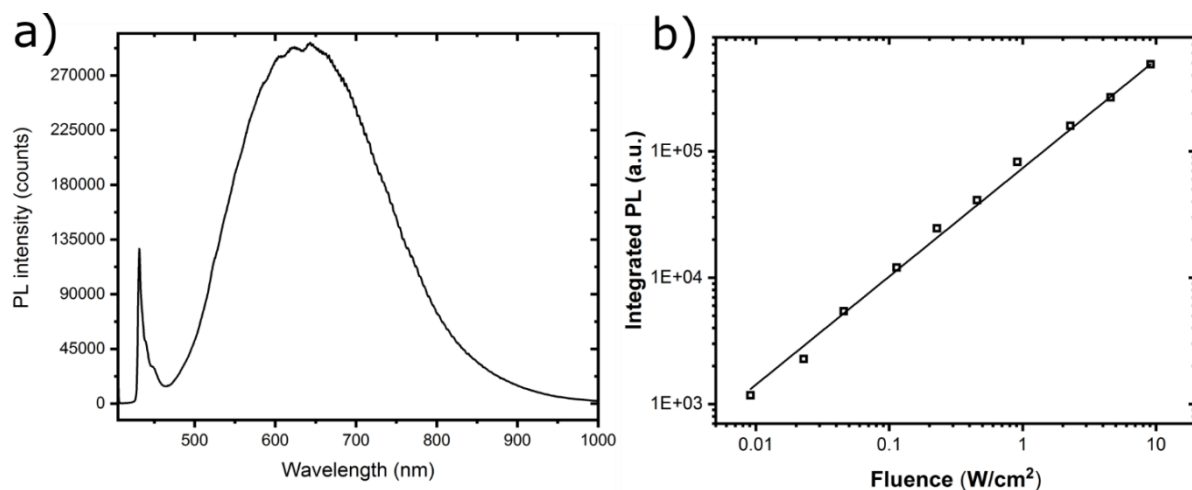
**Figure S6.** Temperature-dependent photoluminescence ( $\lambda_{\text{exc}}=405$  nm) of (a) **1**[PbBr<sub>4</sub>] and (b) **2**[PbBr<sub>4</sub>].



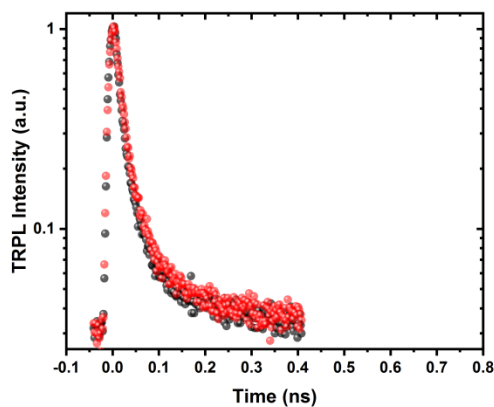
**Figure S7.** Temperature dependence of the (a) full width at half maximum (FWHM) and (b) peak maximum of broadband emission for 1[PbBr<sub>4</sub>] (red points and lines) and 2[PbBr<sub>4</sub>] (blue points and lines).



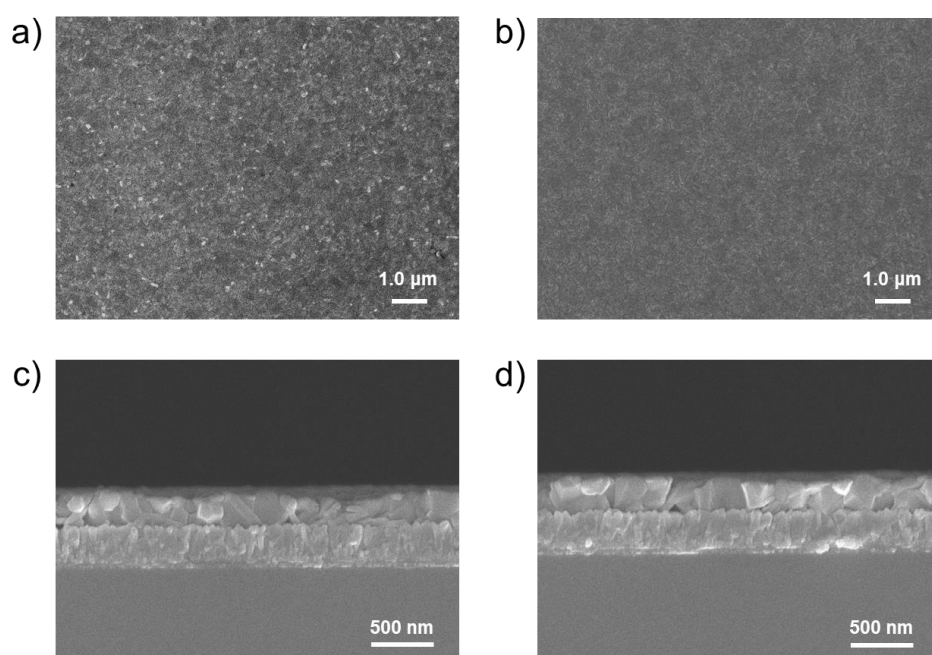
**Figure S8.** Plots of integrated photoluminescence (PL) intensity ( $I$ ) versus the inverse of temperature ( $1/T$ ) for (a) 1[PbBr<sub>4</sub>] and (b) 2[PbBr<sub>4</sub>]. The data was fit to the Arrhenius equation, with inclusion of two competitive nonradiative recombination channels:  $I = I_0 / [1 + C_1 \exp(-Ea_1/kT) + C_2 \exp(-Ea_2/kT)]$ , where  $Ea_1$  and  $Ea_2$  are activation energies for the thermal de-trapping process,  $k$  is the Boltzmann constant,  $I_0$  is extrapolated PL intensity at 0 K, and  $C_1$  and  $C_2$  represent the strength of the quenching processes. The parameters derived from the fit are summarized in Table S5.



**Figure S9.** a) PL spectrum of 1[PbBr], measured at 77K. At this temperature, there is a single excitonic peak at 432 nm, followed by a structured sideband over the range 435 – 460 nm. b) Power dependence of integrated PL intensity for 1[PbBr], measured at 77 K, in the integration range 435 – 460 nm. Sublinear growth with  $k = 0.85 \pm 0.01$  is observed. This power dependence is indicative of the presence of trap states in the low energy tail of the excitonic emission. Since it is not possible to completely separate contributions to PL stemming from the exciton and sub-bandgap states, the power law dependence in the excitonic range emission (428 – 435 nm; see Figure 4a in main text) shows a slight deviation from unity. All data were recorded using single crystals.



**Figure S10.** Room temperature, time-resolved dynamics of the PL emission of 1[PbBr<sub>4</sub>] in the ranges 420 - 440 nm (black spheres) and 440 – 470 nm (red spheres). Data was recorded for single crystals, using an  $\lambda_{\text{ex}}$  of 368 nm. The very similar dynamics of the two bands confirms that they have the same excitonic nature.



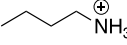
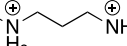
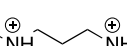

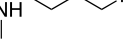
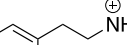

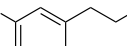

**Figure S11.** Field emission scanning electron micrographs (FE-SEMs) of the surface morphologies and cross sections of thin films of  $1[\text{PbBr}_4]$ , (a) and (c), and  $2[\text{PbBr}_4]$ , (b) and (d). Thin films of the 2D perovskites were obtained by spin coating onto FTO glass substrates.

**Table S1.** Crystallographic and structure refinement data for **1[PbBr<sub>4</sub>]** and **2[PbBr<sub>4</sub>]** at cryogenic and ambient temperatures.<sup>a</sup>

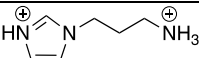
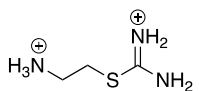
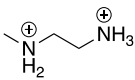
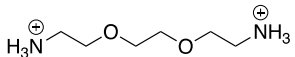
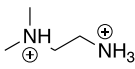
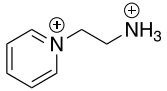
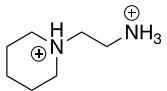
	Compound			
	<b>1[PbBr<sub>4</sub>]</b> (100 K)	<b>2[PbBr<sub>4</sub>]</b> (100 K)	<b>1[PbBr<sub>4</sub>]</b> (RT)	<b>2[PbBr<sub>4</sub>]</b> (RT)
Empirical formula	C <sub>7</sub> H <sub>12</sub> Br <sub>4</sub> N <sub>2</sub> Pb	C <sub>7</sub> H <sub>18</sub> Br <sub>4</sub> N <sub>2</sub> Pb	C <sub>7</sub> H <sub>12</sub> Br <sub>4</sub> N <sub>2</sub> Pb	C <sub>7</sub> H <sub>18</sub> Br <sub>4</sub> N <sub>2</sub> Pb
Formula weight	651.02 g/mol	657.06 g/mol	651.02 g/mol	657.06 g/mol
Wavelength	0.71073 Å	0.71073 Å	0.71073 Å	0.71073 Å
Crystal size	0.020 x 0.040 x 0.120 mm	0.040 x 0.120 x 0.320 mm	0.020 x 0.040 x 0.060 mm	0.020 x 0.120 x 0.200 mm
Crystal habit	yellow needle	colorless plate	pale yellow block	pale yellow plate
Crystal system	orthorhombic	monoclinic	monoclinic	monoclinic
Space group	P b c a	P 1 21/c 1	P 1 21/c 1	P 1 21/c 1
Unit cell dimensions	a = 17.0426(4) Å α = 90° b = 8.2800(2) Å β = 90° c = 19.7640(5) Å γ = 90°	a = 6.1025(2) Å α = 90° b = 19.6991(8) Å β = 97.1920(14)° c = 12.2289(5) Å γ = 90°	a = 10.339(5) Å α = 90° b = 17.223(9) Å β = 105.29(2)° c = 8.346(4) Å γ = 90°	a = 6.1592(2) Å α = 90° b = 19.9946(8) Å β = 95.2440(10)° c = 12.1402(4) Å γ = 90°
Volume	2788.95(12) Å <sup>3</sup>	1458.52(10) Å <sup>3</sup>	1433.6(13) Å <sup>3</sup>	1488.82(9) Å <sup>3</sup>
Z	8	4	4	4
Density	3.101 g/cm <sup>3</sup>	2.992 g/cm <sup>3</sup>	3.016 g/cm <sup>3</sup>	2.931 g/cm <sup>3</sup>
Absorption coefficient	23.529 mm <sup>-1</sup>	22.497 mm <sup>-1</sup>	22.887 mm <sup>-1</sup>	22.039 mm <sup>-1</sup>
F(000)	2320	1184	1160	1184
Theta range for data collection	2.38 to 30.00°	2.66 to 32.00°	2.36 to 31.11°	2.64 to 32.13°
Reflections collected	29677	32046	4563	17677
Coverage of independent reflections	100.00%	100.00%	99.00%	99.60%
Absorption correction	Multi-Scan	Multi-Scan	Multi-Scan	Multi-Scan
Max. and min. transmission	0.6500 and 0.1650	0.4660 and 0.0520	0.6570 and 0.3410	0.6670 and 0.0960
Function minimized	Σ w(F <sub>o</sub> <sup>2</sup> - F <sub>c</sub> <sup>2</sup> ) <sup>2</sup>	Σ w(F <sub>o</sub> <sup>2</sup> - F <sub>c</sub> <sup>2</sup> ) <sup>2</sup>	Σ w(F <sub>o</sub> <sup>2</sup> - F <sub>c</sub> <sup>2</sup> ) <sup>2</sup>	Σ w(F <sub>o</sub> <sup>2</sup> - F <sub>c</sub> <sup>2</sup> ) <sup>2</sup>
Data / restraints / parameters	4071 / 0 / 128	5064 / 0 / 128	4563 / 62 / 122	5206 / 403 / 211
Goodness-of-fit on F <sup>2</sup>	1.04	1.022	1.006	1
Δ/σ <sub>max</sub>	0.002	0.001	0.001	0.001
Final R indices	3076 data	3524 data	2481 data	2431 data
[I > 2σ(I)]	R1 = 0.0319, wR2 = 0.0600	R1 = 0.0371, wR2 = 0.0626	R1 = 0.0633, wR2 = 0.1302	R1 = 0.0572, wR2 = 0.1047
R indices [all data]	R1 = 0.0551, wR2 = 0.0679	R1 = 0.0682, wR2 = 0.0747	R1 = 0.1340, wR2 = 0.1615	R1 = 0.1551, wR2 = 0.1389
Largest diff. peak and hole	1.272 and -1.594 eÅ <sup>-3</sup>	1.649 and -1.947 eÅ <sup>-3</sup>	3.197 and -1.596 eÅ <sup>-3</sup>	1.865 and -2.121 eÅ <sup>-3</sup>
R.M.S. deviation from mean	0.290 eÅ <sup>-3</sup>	0.297 eÅ <sup>-3</sup>	0.274 eÅ <sup>-3</sup>	0.306 eÅ <sup>-3</sup>

<sup>a</sup>R = Σ||F<sub>o</sub> - |F<sub>c</sub>||/Σ|F<sub>o</sub>|, wR = {Σ[w(|F<sub>o</sub> - |F<sub>c</sub>||)<sup>2</sup>]/Σ[w(|F<sub>o</sub>||)<sup>2</sup>]}<sup>1/2</sup> and **1[PbBr<sub>4</sub>]**, w = 1/[σ<sup>2</sup>(F<sub>o</sub><sup>2</sup>) + (0.0240P)<sup>2</sup> + 6.4233P]; **2[PbBr<sub>4</sub>]**, w = 1/[σ<sup>2</sup>(F<sub>o</sub><sup>2</sup>) + (0.0143P)<sup>2</sup> + 6.5277P]; **3[PbBr<sub>4</sub>]**, w = 1/[σ<sup>2</sup>(F<sub>o</sub><sup>2</sup>) + (0.0868P)<sup>2</sup> + 0.9679P]; **4[PbBr<sub>4</sub>]**, w = 1/[σ<sup>2</sup>(F<sub>o</sub><sup>2</sup>) + (0.0346P)<sup>2</sup> + 42.7986P]; **5[PbBr<sub>4</sub>]**, w = 1/[σ<sup>2</sup>(F<sub>o</sub><sup>2</sup>) + (0.0167P)<sup>2</sup>]; **6[PbBr<sub>5</sub>]<sub>2/3</sub>**, w = 1/[σ<sup>2</sup>(F<sub>o</sub><sup>2</sup>) + (0.0493P)<sup>2</sup> + 3.6279P] where P = (F<sub>o</sub><sup>2</sup> + 2F<sub>c</sub><sup>2</sup>)/3.

**Table S2.** Summary of distortion parameters for **1**[PbBr<sub>4</sub>] and **2**[PbBr<sub>4</sub>], plus those of selected (100)-oriented 2D Pb-Br perovskites.

Organic cation	$\Delta d$ ( $\times 10^{-4}$ )	$\lambda_{oct}$	$\sigma_{oct}^2$	Ref.
	0.07	1.0027	9.43	14
	0.50	1.0009	3.03	15
	1.10	1.0119	40.58	16
	4.30	1.0094	32.64	16
	9.77	1.0056	16.35	17
	0.85	1.0060	20.72	14
	2.92	1.0115	36.99	14
	13.66	1.0104	30.09	This work
	9.46	1.0109	33.99	This work

**Table S3.** Summary of distortion parameters for **1**[PbBr<sub>4</sub>] and **2**[PbBr<sub>4</sub>], plus those of selected (110)-oriented 2D Pb-Br perovskites.

Organic cation	$\Delta d$ (x10 <sup>-4</sup> )	$\lambda_{oct}$	$\sigma_{oct}^2$	Ref.
	26.02	1.0088	20.80	18
	9.67	1.0123	38.89	19
	8.20	1.0080	24.51	15
	24.00	1.0090	23.91	20
	17.40	1.0068	17.35	16
	13.66	1.0104	30.09	This work
	9.46	1.0109	33.99	This work

**Table S4.** Summary of distortion parameters for **1**[PbBr<sub>4</sub>] and **2**[PbBr<sub>4</sub>] at cryogenic and ambient temperatures.

Compound	$\Delta d$ (x10 <sup>-4</sup> )	$\lambda_{oct}$	$\sigma_{oct}^2$	$D_{tilt}$ (°)	$D_{out}$ (°)	$D_{in}$ (°)
<b>1</b> [PbBr <sub>4</sub> ] at 100 K	1.0131	36.41	19.59	6.7	6.1	2.8
<b>2</b> [PbBr <sub>4</sub> ] at 100 K	1.0205	62.32	16.57	7.7	4.9	5.9
<b>1</b> [PbBr <sub>4</sub> ] at 296 K	1.0104	30.09	13.65	7.9	6.0	5.1
<b>2</b> [PbBr <sub>4</sub> ] at 296 K	1.0109	33.99	9.46	12.2	10.5	6.2

**Table S5.** List of equatorial Pb-Br bond lengths for **1**[PbBr<sub>4</sub>] and **2**[PbBr<sub>4</sub>] at room temperature.

	<b>1</b> [PbBr <sub>4</sub> ]	<b>2</b> [PbBr <sub>4</sub> ]
	3.022	2.929
	3.025	3.176
	3.028	3.013
	2.987	3.151
Average	3.015	3.067



**Table S6.** Parameters obtained from fits of Figure S8 to the Arrhenius plots.

	$I_0$ [ $\times 10^7$ ]	$Ea_1$ [meV]	$C_1$	$Ea_2$ [meV]	$C_2$ [ $\times 10^4$ ]	$R^2$
<b>1</b> [PbBr <sub>4</sub> ]	$2.3 \pm 0.1$	$41 \pm 1$	$388 \pm 48$	$122 \pm 16$	$2.9 \pm 2.3$	0.999
<b>2</b> [PbBr <sub>4</sub> ]	$1.3 \pm 0.4$	$43 \pm 1$	$216 \pm 32$	$140 \pm 17$	$5.2 \pm 4.8$	0.999

**Table S7.** Parameters obtained from fitting TRPL decay plots.

	Broad component <b>1</b> [PbBr <sub>4</sub> ] at 78 K	Broad component <b>2</b> [PbBr <sub>4</sub> ] at 78 K	Exciton <b>1</b> [PbBr <sub>4</sub> ] at 298 K	Broad component <b>2</b> [PbBr <sub>4</sub> ] at 298 K
$\beta$	0.25024	0.92583	0.69255	0.67013
$\tau$	2.24401 ns	19.03608 ns	0.01521 ns	0.12542 ns

## References

1. SAINT and SADABS; Bruker AXS Inc.: Madison, WI, (2007).
2. Sheldrick, G. M. *SHELXL-97, Program for crystal structure refinement*; Göttingen, **1997**.
3. Sheldrick, G. M. *Acta Crystallogr., Sect. A: Found. Crystallogr.*, **2008**, *64*, 112–122.
4. Momma, K.; Izumi, F. An Integrated Three-Dimensional Visualization System VESTA Using wxWidgets. *Commission on Crystallogr. Comput.*, **2006**, *7*, 106–119.
5. Ertl, A.; Hughes, J. M.; Pertlik, F.; Jr., F. F. F.; Wright, S. E.; Brandstatter, F.; Marler, B. Polyhedron Distortions in Tourmaline. *Can. Mineral.*, **2002**, *40*, 153–162.
6. Robinson, K.; Gibbs, G. V.; Ribbe, P. H. Quadratic Elongation: a Quantitative Measure of Distortion in Coordination Polyhedra. *Science* **1971**, *172*, 567–570.
7. Thomas, N. W. Crystal Structure–Physical Property Relationships in Perovskites. *Acta Crystallographica Section B* **1989**, *45*, 337–344.
8. Fleet, M. E. Distortion Parameters for Coordination Polyhedra. *Mineralogical Magazine* **1976**, *40*, 531–533.
9. Lemmerer, A.; Billing, D. G. *CrystEngComm*, **2010**, *12*, 1290–1301.
10. S. Zhang, G. Lanty, J.-S. Lauret, E. Deleporte, P. Audebert and L. Galmiche, *Acta Materialia*, **2009**, *57*, 3301–3309.
11. K. Pradeesh, K. Nageswara Rao and G. Vijaya Prakash, *J. Appl. Phys.*, 2013, **113**, 083523.
12. Du, K. Z.; Tu, Q.; Zhang, X.; Han, Q.; Liu, J.; Zauscher, S.; Mitzi, D. B., *Inorg. Chem.* **2017**, *56* (15), 9291–9302.
13. Leguy, A. M.; Goni, A. R.; Frost, J. M.; Skelton, J.; Brivio, F.; Rodriguez-Martinez, X.; Weber, O. J.; Pallipurath, A.; Alonso, M. I.; Campoy-Quiles, M.; Weller, M. T.; Nelson, J.; Walsh, A.; Barnes, P. R., *Phys Chem Chem Phys* **2016**, *18* (39), 27051–27066.
14. Smith, M. D.; Jaffe, A.; Dohner, E. R.; Lindenberg, A. M.; Karunadasa, H. I. Structural Origins of Broadband Emission from Layered Pb–Br Hybrid Perovskites. *Chem. Sci.*, **2017**, *8*, 4497–4504.
15. Dohner, E. R.; Hoke, E. T.; Karunadasa, H. I. Self-Assembly of Broadband White-Light Emitters. *J. Am. Chem. Soc.*, **2014**, *136*, 1718–1721.
16. Mao, L.; Wu, Y.; Stoumpos, C. C.; Wasielewski, M. R.; Kanatzidis, M. G. White-Light Emission and Structural Distortion in New Corrugated Two-Dimensional Lead Bromide Perovskites. *J. Am. Chem. Soc.*, **2017**, *139*, 5210–5215.

17. Shibuya, K.; Koshimizu, M.; Nishikido, F.; Saito, H.; Kishimoto, S.  
Poly[bis(phenethylammonium) [dibromidoplumbate(II)]-di-1-bromido]]. *Acta Crystallogr., Sect. E: Struct. Rep. Online*, **2009**, *65*, m1323–m1324.
18. Li, Y.Y.; Lin, C. K.; Zheng, G. L.; Cheng, Z. Y.; You, H.; Wang, W. D.; Lin, J. Novel <110>-Oriented Organic–Inorganic Perovskite Compound Stabilized by *N*-(3-Aminopropyl)imidazole with Improved Optical Properties. *Chem. Mater.*, **2006**, *18*, 3463–3469.
19. Li, Y.; Zheng, G.; Lin, J. Synthesis, Structure, and Optical Properties of a Contorted <110>-Oriented Layered Hybrid Perovskite: C<sub>3</sub>H<sub>11</sub>SN<sub>3</sub>PbBr<sub>4</sub>. *Eur. J. Inorg. Chem.*, **2008**, 1689–1692.
20. Dohner, E. R.; Jaffe, A.; Bradshaw, L. R.; Karunadasa, H. I. Intrinsic White-Light Emission from Layered Hybrid Perovskites. *J. Am. Chem. Soc.*, **2014**, *136*, 13154–13157.